

Optical properties of sub-wavelength hole arrays in SiC membranes

Y A Urzhumov^{1,3}, D Korobkin¹, B Neuner III¹, C Zorman² and G Shvets¹

¹ Department of Physics, The University of Texas at Austin, Austin, TX 78712, USA

² Department of Electrical Engineering, Case Western Reserve University, Cleveland, OH 44106, USA

E-mail: yar@physics.utexas.edu

Received 16 March 2007, accepted for publication 2 May 2007

Published 22 August 2007

Online at stacks.iop.org/JOptA/9/S322

Abstract

It is shown that perforated SiC membranes can be used for engineering optical properties of metamaterials in the infrared. The complex-valued frequency-dependent effective dielectric permittivity $\epsilon_{\text{eff}}(\omega)$ of a single membrane can be controlled by the size and spacing between the holes. Regions of the anomalous dispersion and strong absorption described by $\epsilon_{\text{eff}}(\omega)$ have been identified and related to the excitation of even-parity surface phonon polaritons of a smooth SiC film. The effective permittivity description has been validated by comparing the transmittance and absorbance of the film obtained from $\epsilon_{\text{eff}}(\omega)$ with that calculated using first principles electromagnetic simulations. Theoretical predictions of the enhanced transmission and absorption in the perforated film have been verified experimentally using FTIR micro-spectroscopy. For the first time, the dependence of enhanced transmission and absorption on the incidence plane of the incoming radiation has been studied.

Keywords: metamaterial, effective medium, electrostatic, plasmonic, resonance, phonon–polariton, silicon carbide, thin film, perforated membrane, hole array, extraordinary transmission

(Some figures in this article are in colour only in the electronic version)

1. Introduction

A sub-wavelength hole in a metallic screen is one of the simplest objects in nano-optics. The calculation of light transmission through a single hole in a thin, perfectly conducting screen was one of the first analytically solved problems in sub-wavelength optics. Bethe's famous result [1] indicated that the transmission coefficient through a sub- λ hole is extremely low: it rapidly decays with the hole diameter D as $(D/\lambda)^6$, where λ is the wavelength of light. This low transmission considerably diminished the perceived utility of a nanohole as a nanophotonic device. However, a real metallic screen is neither perfectly conducting nor infinitely thin. Nor must the nanoholes be isolated: they can form periodic or quasi-periodic arrays. A new surge

of interest in nanoholes followed the remarkable discovery by Ebbesen and collaborators [2] of extraordinary optical transmission (EOT) through sub- λ periodic hole arrays. The original experiments were done using optically thick substrates for which the extraordinary transmission is most dramatic: no light is transmitted through the films in the absence of holes but, contrary to Bethe's prediction, a rather significant transmission was observed when the sub-wavelength hole array was present. A number of analytic tools based on EOT are already under development [3], including refractive index sensors [4], infrared absorption spectroscopy sensors [5], and multispectral biosensors [6].

The enhanced transmission was attributed to resonant excitation of surface plasmons. The role of surface plasmons in the enhanced transmission was questioned in a number of subsequent publications [7, 8] and still remains a subject

³ Author to whom any correspondence should be addressed.

of some controversy. The main reason for this controversy is that several complicated phenomena are playing out in EOT experiments. In addition to surface plasmons, more conventional diffractive and interference phenomena such as waveguide resonances [7, 9], Wood's anomalies, and quasi-bound modes [10] were shown to contribute to (or in some instances be the sole cause of) the extraordinary transmission. For example, extraordinary transmission has been observed at terahertz and even microwave frequencies, for which surface plasmons do not exist [11, 12]. It was later theoretically demonstrated [13] that holes and other perforations in a thick perfectly conducting metal (which do not support the 'true' surface plasmons) can support the so-called 'spoof plasmons'. In an optical experiment similar to the original EOT work, all these effects (surface plasmons, 'spoof plasmons', Wood's anomalies, waveguide resonances) occur at the same time because the EOT wavelength is very close to the Wood's anomaly: $\lambda \approx \sqrt{\epsilon_d}L$, where L is the array's periodicity and ϵ_d is the dielectric permittivity of the substrate that supports the metal film.

In this paper, we describe a series of experiments (supported by theoretical calculations and first-principles electromagnetic simulations) enabling us to clearly separate EOT due to diffractive effects from the EOT due to the excitation of surface polaritons (SPs). In this report, the general term *polariton* refers to either plasmon polaritons or phonon polaritons. First, the perforated films are optically thin, ruling out 'spoof polaritons'. Second, all measurements are carried out in the mid-infrared part of the spectrum, with the films made of silicon carbide (SiC). SiC is a low-loss polaritonic material that has a negative dielectric permittivity $\epsilon(\omega)$ for a range of frequencies referred to as the *reststrahlen* band. Therefore, the surface polaritons responsible for mid-IR EOT are the surface phonon polaritons (SPPs). Because SiC films are thin ($\lambda_{\text{skin}} \equiv \lambda/4\pi\sqrt{|\epsilon|} > H$), the SPPs responsible for EOT are double-sided polaritons, i.e., they exist on both SiC–vacuum interfaces. Third, the high-index substrate is eliminated by using air-bridged (suspended) SiC membranes, thereby ensuring that EOT is observed far from the grazing-angle (Wood's) anomalies at the substrate–film interface. This enables us to observe EOT in the sub-wavelength regime ($D \ll \lambda$ and $L < \lambda$), where only SPPs and not diffractive effects can be responsible for EOT.

Using polarized FTIR micro-spectroscopy and detecting both transmitted and reflected radiation, we demonstrate, in adjacent frequency ranges, extraordinary optical transmission and absorption of the incident radiation. Our theoretical calculations and numerical simulations show that both phenomena are caused by the excitation of quasi-electrostatic SPPs. It is shown that a perforated film can be described as a *metamaterial* with the effective permittivity $\epsilon_{\text{eff}} = \epsilon_r + i\epsilon_i$ strongly modified by the excitation of SPPs. Armed with ϵ_{eff} , transmission and reflection coefficients T and R can be determined using Fresnel formulas for a dielectric slab. Regions of the enhanced transmission and absorption are related, respectively, to the lowering of $|\epsilon_r|$ and increase of ϵ_i .

We show that SPPs supported by the perforated film give rise to the poles of the ϵ_{eff} , which becomes substantially different from $\epsilon(\omega)$ of the smooth SiC film in the vicinity of SPP resonances. The effective permittivity description

is enabled by the sub-wavelength nature of the perforated membranes. We demonstrate that only the slow surface polaritons (SSPs) whose in-plane electric field is even with respect to the mid-plane of the film contribute to the effective permittivity. The role of SPPs in EOT can be phenomenologically interpreted as Fano [14, 15] resonances. The first-principles explanation of the enhanced transmission and absorption using a quasi-static $\epsilon_{\text{eff}} \equiv \epsilon_{\text{qs}}$ developed in section 2 removes the phenomenological aspect of the interpretation based on Fano resonances. In addition, we theoretically show that two types of SPPs are supported by the hole arrays in a polaritonic membrane: localized surface polaritons (LSPs) and delocalized SSPs. The LSPs are shown to exist inside the frequency band corresponding to $-1 < \epsilon(\omega) < 0$, where they cannot decay into propagating SPPs.

The remainder of the paper is organized as follows. Section 2 describes our theoretical approach to modelling EOT by introducing a frequency-dependent effective dielectric permittivity of the perforated membrane $\epsilon_{\text{eff}}(\omega)$ in the electrostatic (ES) approximation. Transmission and reflection coefficients obtained from $\epsilon_{\text{eff}}(\omega)$ are compared to the results of full electromagnetic simulations. In section 3, SPPs supported by a perforated plasmonic or polaritonic film and responsible for the EOT are classified and their relation to the SPPs supported by a smooth (unperforated) film is investigated. Red-shifting of the absorption and transmission peaks from the spectral position of smooth film SPPs is explained. In section 4, experimental results are described. The details of the perforated SiC film fabrication are described in section 4.1, the polarized FTIR micro-spectroscopy set-up is described in the first half of section 4.2, and the measurements of the dielectric permittivity $\epsilon(\omega)$ of the thin smooth (unperforated) SiC film are described in the second half of section 4.2. Experimental measurements of the enhanced transmission and absorption through perforated SiC membranes are described in section 4.3. The measurements for the two incident light polarizations (s and p), as well as the dependence of EOT on the incidence plane of the incoming beam, are described.

2. Effective optical constants of nanostructures in the quasi-static approximation

In this section we describe theoretical techniques that can be used to characterize three-dimensional metamaterials with sub-wavelength features (characteristic feature size much smaller than the wavelength of light in vacuum). Our approach relies on the quasi-static approximation, which assumes that a patterned metamaterial (such as, in our case, an SiC film perforated by a hole array) can be described by a quasi-static dielectric permittivity $\epsilon_{\text{qs}}(\omega)$ obtained by solving an electrostatic problem [16–18] of the material's response to an imposed electric field $\vec{E}_0(\vec{r}, t) = \vec{E}_0 e^{-i\omega t}$. The electrostatic problem can be expressed as

$$\nabla \epsilon(\vec{r}, \omega)(-\vec{\nabla} \phi) = 0, \quad (1)$$

where the total electric field $\vec{E} = -\vec{\nabla} \phi$ is excited by a slowly oscillating external field $\vec{E}_0 \equiv -\vec{\nabla} \phi_0$. For equation (1) it implies that $\phi - \phi_0$ satisfies periodic boundary conditions. Owing to the periodicity and symmetry of the perforated

membrane, it is sufficient to solve equation (1) inside the unit cell. Because we are mostly concerned with the small incidence angle transmission, only the in-plane component of the permittivity tensor will be of interest. Therefore, $\vec{E}_0 = E_0 \vec{e}_x$, where the film is parallel to the x - y plane, will be assumed.

Equation (1) can be solved directly for a range of ω' values. The quasi-static permittivity $\epsilon_{qs}(\omega)$ is extracted from the solutions by requiring that the electric dipole moment \vec{d} of a unit cell is equal to that of a homogeneous medium with the permittivity tensor $\hat{\epsilon}_{qs}$ immersed in an external field \vec{E}_0 :

$$\vec{d} = \int dV \frac{\epsilon(\vec{r}) - 1}{4\pi} \vec{E}(\vec{r}) \equiv \frac{\hat{\epsilon}_{qs} - \hat{1}}{4\pi} \vec{E}_0 V, \quad (2)$$

where V is the volume of the unit cell. Note that this definition is equivalent to the general result of homogenization theory of differential equations with periodic coefficients [19, 20]. However, additional insights can be gained by reformulating equation (1) as a generalized eigenvalue differential equation (GEDE). A series of electrostatic resonances [16–18] is found, each of which contributes to the metamaterial's response to the external electric field according to its electric dipole strength. The GEDE method has been successfully applied to periodic sub- λ crystals consisting of interpenetrating positive- ϵ dielectrics [21], or non-connected polaritonic inclusions [18]. To our knowledge, this is the first application of this method to the system with *continuous polaritonic* (negative-permittivity) phase, which supports *delocalized surface phonon polaritons*. The steps of the GEDE approach as applied to periodic nanostructures consisting of two material components (one with a frequency-dependent $\epsilon(\omega) < 0$ and another with $\epsilon_d = 1$) are briefly described below, with the details appearing elsewhere [16, 18].

First, the GEDE $\vec{\nabla} \cdot [\theta(\vec{r}) \vec{\nabla} \phi_n] = s_n \nabla^2 \phi_n$ is solved for the real eigenvalues s_n , where $\theta(\vec{r}) = 1$ inside the polaritonic material and $\theta(\vec{r}) = 0$ elsewhere, and ϕ_n are dipole-like potential eigenfunctions periodic in the plane of the film. Examples of several potential functions are given in figure 4. Spectral properties of the GEDE are discussed in detail in [16]. For our purposes it suffices to know that all eigenvalues s_n are real and confined to the segment $0 \leq s \leq 1$. Second, the solution of equation (1) is expressed as [16]

$$\phi(\vec{r}) = \phi_0(\vec{r}) + \sum_n \frac{s_n}{s - s_n} \frac{(\phi_n, \phi_0)}{(\phi_n, \phi_n)} \phi_n(\vec{r}), \quad (3)$$

where the scalar product is defined as $(\phi, \psi) = \int dV \theta \vec{\nabla} \phi^* \cdot \vec{\nabla} \psi$, $\phi_0 = -E_0 x$ represents the external field, and $s \equiv [1 - \epsilon(\omega)]^{-1}$ is a frequency label. Third, the quasi-static permittivity is calculated by substituting $\phi(\vec{r})$ from equation (3) into equation (2):

$$\epsilon_{qs}^{ij} = \delta_{ij} - \frac{1}{s} \left(\frac{V_p}{V} \delta_{ij} - \frac{1}{V} \sum_n \frac{(\phi_n, x_i)^* (\phi_n, x_j)}{(\phi_n, \phi_n)} \right) - \frac{1}{V} \sum_n \frac{(\phi_n, x_i)^* (\phi_n, x_j)}{(\phi_n, \phi_n)(s - s_n)}, \quad (4)$$

where $V_p = \int dV \theta$ is the volume of plasmonic (polaritonic) phase contained within the volume V of a unit cell.

Since our structure has three orthogonal planes of symmetry ($x = 0$, $y = 0$ and $z = 0$), the dielectric tensor is diagonal. Moreover, $\epsilon_{qs}^{xx} \equiv \epsilon_{qs}^{yy}$, because z is the fourfold axis of symmetry:

$$\epsilon_{qs}^{xx} = \epsilon_{qs}^{yy} \equiv \epsilon_{qs}(\omega) = 1 - \frac{f_0}{s(\omega)} - \sum_{n>0} \frac{f_n}{s(\omega) - s_n}, \quad (5)$$

where $f_n = |(\phi_n, x)|^2 / [V(\phi_n, \phi_n)]$ ($n > 0$) is the electric dipole strength of the n th resonance, and $f_0 = V_p/V - \sum_{n>0} f_n$. Using identities $\int dV D_x = \oint dAx (\vec{D} \cdot \vec{n})$ and $\int dV E_x = V E_0$, equation (2) can be expressed in a surface integral form:

$$\oint dAx (\vec{D} \cdot \vec{n}) = \epsilon_{qs}^{xx} E_0 V, \quad (6)$$

where $\vec{D} = \epsilon \vec{E}$. The surface integral in equation (6) is proportional to the charge on the imaginary ‘capacitor plates’ located at the $x = \pm L/2$ boundaries of the unit cell. From equation (6), an alternative expression for the residue f_0 is derived:

$$f_0 = q^{xx} - \frac{1}{V} \sum_n \frac{(\phi_n, x)}{(\phi_n, \phi_n)} \oint dA \theta x \frac{\partial \phi_n}{\partial n}, \quad (7)$$

where $\partial/\partial n$ is the normal derivative and $q^{xx} = \frac{1}{V} \oint dA \theta x \frac{\partial x}{\partial n}$ is the fractional area of the equipotential ($x = \text{constant}$) boundaries occupied by the plasmonic phase. The non-negative quantity f_0 vanishes if the plasmonic phase of the metamaterial does not form a continuous path in the direction of the applied electric field, a path that would connect the ‘capacitor plates’ and enable the current flow [22]. The new expression (7) for the residue f_0 provides analytical proof of this previously noted fact. We observe that the surface integrals in (7), as well as q^{xx} , vanish whenever the boundary of a unit cell does not cross the polaritonic phase. It is evident that a repeating unit cell can always be chosen in a non-percolating polaritonic crystal so as to avoid any intersections with polaritonic particles, even though in densely packed crystals it might be necessary to choose a non-rectangular, non-convex unit cell different from the traditional Wigner–Seitz shape. Thus, the pole of ϵ_{qs} at $s = 0$ exists if and only if the negative- ϵ phase is continuous. Note that in the limit of the smooth film $f_0 = 1$, $f_n = 0$ for $n > 0$, and $\epsilon_{qs}(\omega) \equiv \epsilon(\omega)$. While the oscillator strengths f_n ($n > 0$) can be computed numerically from their corresponding eigenfunctions ϕ_n , calculating f_0 requires a detailed knowledge of all the f_n (or ϕ_n).

An alternative method of calculating f_0 and the f_n is to directly solve equation (1) assuming a uniform electric field \vec{E}_0 , and then to substitute the solution $\phi(\vec{r})$ into equations (2) or (6) defining $\hat{\epsilon}_{qs}$. We used the commercial finite-element solver COMSOL to calculate the quasi-static response of perforated films for experimentally relevant parameters. Because the most dramatic results were obtained for the samples with thickness $H = 458$ nm, period $L = 7$ μm , and hole diameter $D = 2$ μm , all theoretical calculations (except the ones shown in figures 1 and 5, where the period and hole diameter varied) were done for these specific dimensions of the hole array. Also, the following expression for the dielectric

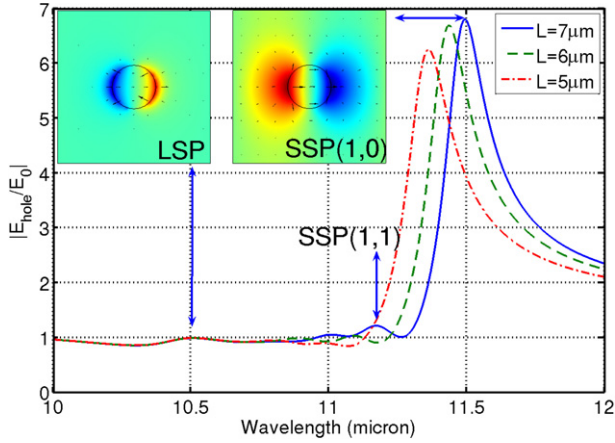


Figure 1. Volume-averaged electric field enhancement inside a hole in a SiC film. Sample: $H = 458$ nm SiC film perforated with a $L = 7 \mu\text{m}$ square array of $D = 2 \mu\text{m}$ round holes (solid line). Insets, ES potential profile at the resonances: left, LSP resonance, and right, SSP(1, 0) resonance. Dashed line, $L = 6 \mu\text{m}$; dash-dotted line, $L = 5 \mu\text{m}$.

permittivity of a doped (with a finite conductivity σ) SiC film has been used:

$$\epsilon_{\text{SiC}}(\omega) = \epsilon_{\infty} \frac{\omega^2 - \omega_{\text{LO}}^2 + i\Gamma\omega}{\omega^2 - \omega_{\text{TO}}^2 + i\Gamma\omega} + \frac{i\sigma}{\omega}, \quad (8)$$

where $\omega_{\text{LO}} = 972 \text{ cm}^{-1}$ ($\lambda_{\text{LO}} = 10.288 \mu\text{m}$), $\omega_{\text{TO}} = 796 \text{ cm}^{-1}$ ($\lambda_{\text{TO}} = 12.563 \mu\text{m}$), $\Gamma = 5.25 \text{ cm}^{-1}$, $\sigma = 346.2 \text{ cm}^{-1}$, and $\epsilon_{\infty} = 4.71$ were found to give the best fit to the experimental transmission data for the unperforated membrane as explained in section 4.2.

Real and imaginary parts of $\epsilon_{\text{qs}}(\omega)$ are plotted in figure 2. The strongest electrostatic resonance can be clearly identified as the maximum of $\text{Im}[\epsilon_{\text{qs}}(\omega)]$. The extracted $\epsilon_{\text{qs}}(\omega)$ can be fitted to equation (5) to determine the dipole oscillator strengths f_0 and f_n as well as their spectral positions ω_n corresponding to $s(\omega_n) = s_n$. The following values of the electrostatic eigenvalues s_n and electric dipole strengths f_n of the dominant dipole resonances were found to be $s_0 = 0$ ($\epsilon_0 = -\infty$) with $f_0 \approx 0.88$, $s_1 \approx 0.1241$ ($\epsilon_1 \approx -7.058$) with $f_1 \approx 0.041$ (the strongest resonance), $s_2 \approx 0.1958$ ($\epsilon_2 \approx -4.107$) with $f_2 \approx 0.0054$, $s_3 \approx 0.255$ ($\epsilon_3 \approx -2.922$) with $f_3 \approx 0.0036$, and $s_4 \approx 0.666$ ($\epsilon_4 \approx -0.50$) with $f_4 \approx 0.0049$.

To better identify different contributing resonances of the structure, we have calculated electric field E_{hole} (averaged over the volume of a hole) in response to ac electric field E_0 , as a function of frequency. The ratio of E_{hole}/E_0 is plotted in figure 1 for a fixed hole diameter $D = 2 \mu\text{m}$ and variable period L . Four enhancement spikes corresponding to resonances of $\epsilon_{\text{qs}}(\omega)$ can be identified for all periods. By comparing figures 1 and 2 we note that some of the resonances that are manifest in the field enhancement pictures (second and third from the right in figure 1) barely contribute to the effective dielectric permittivity ϵ_{qs} . That is due to several factors, for example high localization of the enhanced fields or cancellation between the fields in different parts of the structure, or even the enhancement of the *orthogonal*

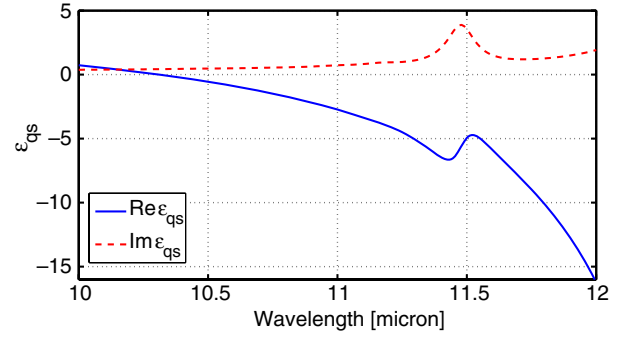


Figure 2. Real (solid line) and imaginary (dashed line) parts of effective quasi-static permittivity of a perforated SiC film (electrostatic FEM simulation). Sample: $H = 458$ nm SiC film perforated with a $L = 7 \mu\text{m}$ square array of $D = 2 \mu\text{m}$ round holes.

component of the electric field. These effects can be appreciated from the potential plots for different resonances in figure 4. More detailed discussion of the electrostatic resonances is found in section 3.

Once the effective permittivity $\epsilon_{\text{qs}}(\omega)$ is known, one can estimate the transmission (T) and reflection (R) coefficients of the sub-wavelength array using well known formulas for a homogeneous slab. At normal incidence, these formulas read

$$T = \left| \frac{(1 - r_1^2) e^{ik_0(n-1)H}}{1 - r_1^2 e^{2ik_0nH}} \right|^2, \quad (9)$$

$$R = \left| \frac{r_1(1 - e^{2ik_0nH})}{1 - r_1^2 e^{2ik_0nH}} \right|^2,$$

where $n = \sqrt{\epsilon_{\text{qs}}}$, $k_0 = \omega/c$ and $r_1 = (1 - n)/(1 + n)$.

We have calculated transmittance T and absorbance $A = 1 - R - T$ of the perforated film, subtracted the corresponding quantities for the non-perforated film (ϵ_{qs} replaced by ϵ_{SiC}), and plotted the corresponding differential quantities in figure 3. The absorption spike (red dashed line) is caused by the peak of $\text{Im}[\epsilon_{\text{qs}}]$ at $\lambda = \lambda_1 \approx 11.45 \mu\text{m}$ in the quasi-static approximation, and corresponds to the resonant frequency. The transmission maximum occurs because of the decrease of the absolute value $|\text{Re}[\epsilon_{\text{qs}}]|$ (with the rise of $\text{Re}[\epsilon_{\text{qs}}] < 0$) at $\lambda = \lambda_{\text{max}} \approx 11.6 \mu\text{m}$, as seen in figure 2. In agreement with the Lorentz theory of resonant response, this rise of $\text{Re}[\epsilon_{\text{qs}}] < 0$ takes place below the resonance frequency. Enhanced transmission predicted from ϵ_{qs} thus occurs for $\lambda_{\text{max}} > \lambda_1$ —slightly red-shifted from the enhanced absorption band. Because spacing between the holes ($L = 7 \mu\text{m}$) is nearly comparable with the wavelength ($\lambda \sim 11 \mu\text{m}$), the quasi-static ϵ_{qs} is only an approximate description of the perforated film. Therefore, fully electromagnetic (EM) calculations of T and A were executed using the finite-element frequency domain (FEFD) solver COMSOL. The results displayed in figure 3 (solid lines) show qualitative agreement with the ϵ_{eff} -based calculation, with the exception that all transmission and absorption maxima are slightly red-shifted. This red-shift is a previously noted [23] effect explained by the EM corrections to the purely ES response of sub- λ polaritonic structures.

To summarize the theoretical results presented in figure 3, we have found that extraordinary transmission through optically thin perforated SiC membranes can be explained

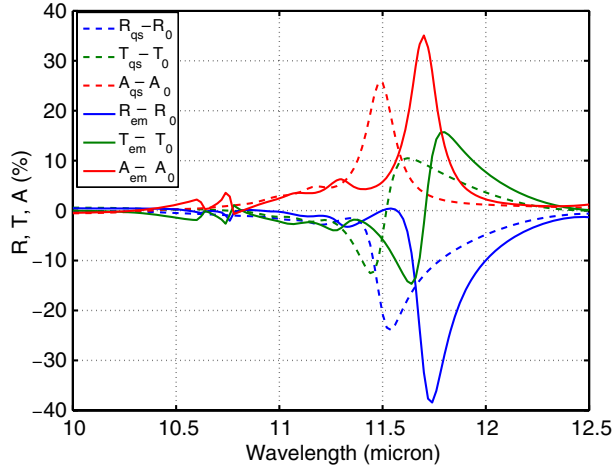


Figure 3. Theory: reflectance (R , blue lines), transmittance (T , green lines) and absorbance (A , red lines) of a perforated SiC film, relative to the same quantities of a smooth film. Solid lines, first-principles FEFD simulation of EM wave scattering; dashed lines, theoretical estimate based on ϵ_{qs} (see figure 2).

using the concept of the effective dielectric permittivity of the sub-wavelength metamaterial. As figure 2 indicates, sub- λ holes introduce a significant (and disproportionate to their overall surface area of under 6%) correction to the dielectric permittivity of the smooth film creating strong resonant features in $\epsilon_{qs}(\omega)$. The strongest modification occurs in the imaginary part of ϵ_{qs} . The physical origin of this modification is the excitation of electrostatic (or quasi-electrostatic when $L/\lambda \sim 1$) resonances. The prominent reduction of the absolute value $|\text{Re}[\epsilon_{qs}]|$ due to the excitation of the strongest resonance results in the prediction of an additional transmittance of 15%—more than twice the geometric area of the holes. Even more dramatically, absorbance is predicted to increase by 35% (from less than 1%). These theoretical predictions are fully confirmed by our experiments as detailed in section 4.3. Below we investigate the nature of quasi-electrostatic resonances that have been shown above to shape the transmission and absorption properties of sub- λ hole arrays in SiC films and relate them to the better known SPPs supported by smooth films.

3. Connection of resonances of a perforated film to surface polaritons of a smooth film

Surface polaritons have been suspected of playing an important role in EOT ever since its discovery [2]. Polarization and dispersion properties of SPs responsible for transmission resonances have been subsequently explored experimentally [4, 24, 25] and theoretically [14, 15] for thick films, and their connection to the SPs of smooth (unperforated) films has been noted. The connection is made by wavenumber matching: resonances of a perforated film with period L are commonly related to SPs of a smooth film with the in-plane wavenumbers $k_{(m,n)} = |\frac{2\pi}{L}(m\hat{x} + n\hat{y})| \equiv \frac{2\pi}{L}\sqrt{m^2 + n^2}$, where m and n are integers. Resonant effects such as enhanced transmission and absorption [24] are expected to occur at frequencies close to those of the smooth film surface polaritons

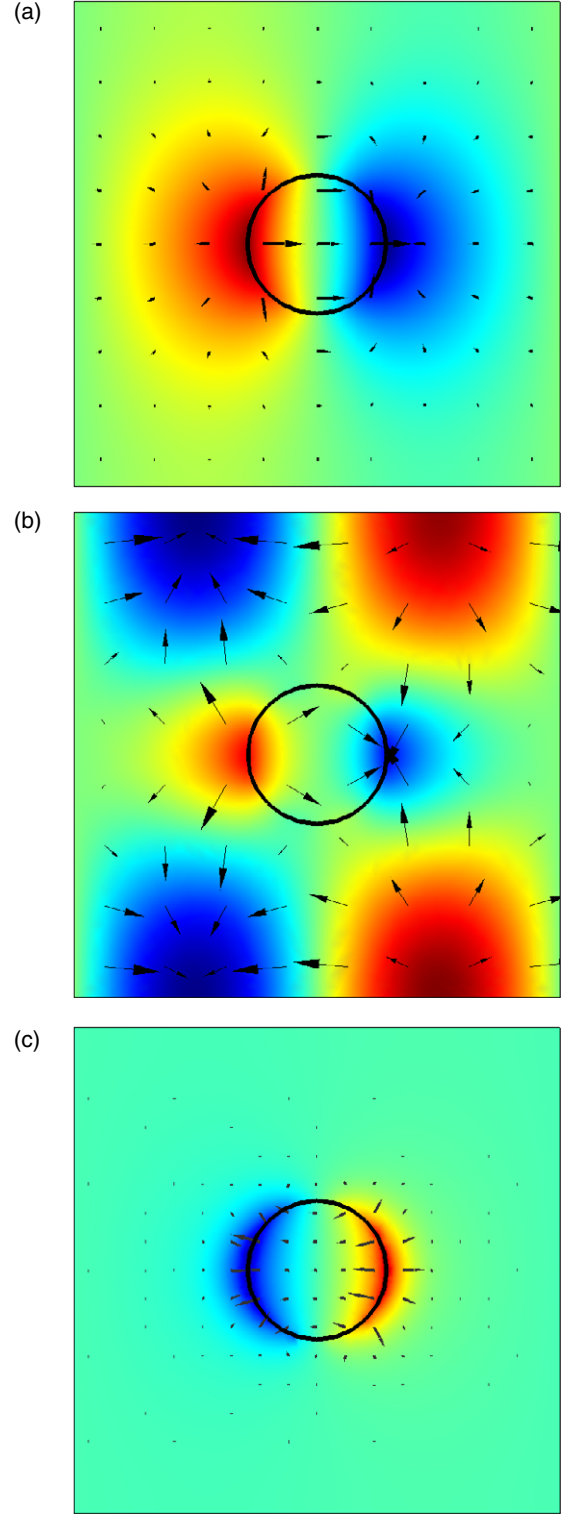


Figure 4. Electrostatic potential and electric field profiles in the mid-plane of quasi-static dipolar eigenmodes of a perforated film (the same as in figure 2). (a) Delocalized resonance corresponding to SSP(1, 0); (b) SSP(1, 1); (c) single-hole resonance (LSP).

$\omega_{SP}(k_{(m,n)})$. For optically thick films, the k -dependent SP frequency is given by an implicit formula, $ck\sqrt{1 + \epsilon^{-1}(\omega_{SP})}$; a slightly more complicated formula for the frequency of *slow*

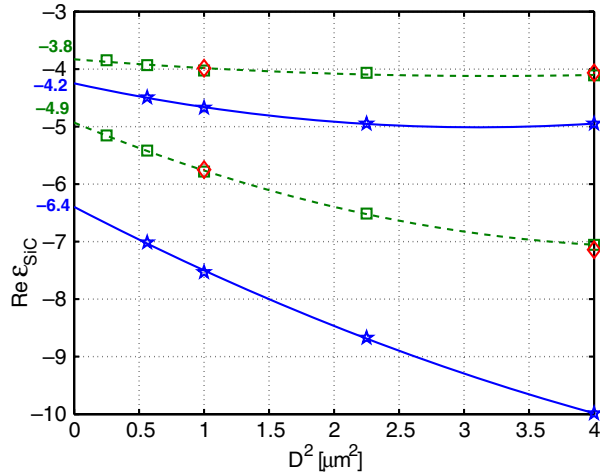


Figure 5. Position of delocalized resonances SSP(1, 0) and SSP(1, 1) as a function of hole diameter D . Squares—position of absorption lines in quasi-static 3D simulations (interpolated with dashed curves); diamonds—electrostatic GEDE simulations; stars—absorption lines in EM FEFD simulations (interpolated with solid curves). Extrapolation to $D = 0$ is also shown.

surface polaritons must be used for thin films. The in-plane component of the electric field of the SSP is even with respect to the mid-plane of the film. In the electrostatic limit ($L \ll \lambda$), $\omega_{\text{SP}}(k)$ is given implicitly by $\epsilon(\omega_{\text{SP}}(k)) = -\tanh^{-1}(kH/2)$.

When the size of the holes becomes of the same order as the period, resonance frequencies are likely to get significantly shifted from their smooth-film values of $\omega_{\text{SP}}(k_{(m,n)})$. This frequency shift has been noted in a number of experiments [14, 26, 27] and attributed to scattering of SPs into light. We find that in the sub-wavelength (quasi-electrostatic) regime there is another reason for the red-shifting of the EOT maximum: the electrostatic resonances are hole-size dependent, explained in detail below. First, we have solved the GEDE equation to obtain several electrostatic resonances, shown in figure 4. The lowest-frequency SSPs can be identified as modified by the presence of a large-hole SSP(1, 0) and SSP(1, 1). Qualitatively, this identification can be made by the visual inspection of figures 4(a) and (b), where the electrostatic potential and electric field in the mid-plane of the perforated film are shown.

To make this identification more quantitative, we have decomposed the electrostatic potential into 2D sin/cos Fourier series. The strongest ES resonance, shown in figure 4 (a), is dominated by the Fourier component $\sin(kx)$, where $k = 2\pi/L$, thus justifying its identification with the SSP(1, 0) of the smooth film. The second strongest resonance, shown in figure 4(b), has a dominant Fourier component $\sin(kx) \cos(ky)$ corresponding to the SSP(1, 1), although it is appreciably hybridized with higher order SSPs. The third strongest resonance, visible in figure 1 (not shown in figure 4), is a mixture of several Fourier components $\sin(mkx) \cos(nky)$ with $m = 1, 2$ and $n = 0, 1, 2$. Mixing between different smooth film polaritons is thus more prominent for shorter-wavelength modes. It appears that surface polaritons with the wavelength comparable to or less than the hole diameter D are more strongly hybridized due to the presence of the

holes. The ES resonances of the perforated film—originating from SSPs of the smooth film—occupy a significant volume of the film, and, more importantly, their frequency is clearly period dependent (see figure 1); therefore, we refer to these ES resonances as delocalized SSPs. Frequencies of all delocalized resonances (field enhancements due to the three strongest are shown in figure 1) are located in the spectral region where $\text{Re}[\epsilon_{\text{SiC}}] < -1$. This is expected because this spectral interval corresponds to *propagating* slow surface polaritons.

We have investigated the frequency dependence of delocalized resonances on the hole diameter D . Resonance positions corresponding to $D = 0$ (smooth film) were obtained by interpolation. Noting that $\text{Re}[\epsilon]$ is a monotonic function of the frequency ω and using $\text{Re}[\epsilon(\omega)]$ as a frequency label, we have used GEDE to compute the spectral positions of the electrostatic delocalized resonances (dashed lines in figure 5) SSP(1, 0) and SSP(1, 1). A significant red-shifting of the strongest electrostatic SSP(1, 0) resonance is observed: $\Delta\epsilon^{(\text{ES})} \approx -2$ as the hole diameter increases from $D = 0$ (smooth film) to $D = 2 \mu\text{m}$ (perforated film). From the first-principles FEFD simulations we have also calculated the values of $\text{Re}[\epsilon]$ as a function of the hole diameter for which an absorption peak is observed (solid lines). Even for the smooth film, electromagnetic resonances are red-shifted with respect to their electrostatic counterparts because the array period $L = 7 \mu\text{m}$ is comparable to the wavelength, and the electrostatic calculation is only approximately valid. The red-shift between the electrostatic and electromagnetic resonances increases as holes get larger, arguably [14, 27] due to radiation from the holes. According to the FEFD simulations, for $D = 2 \mu\text{m}$ holes the amount of red-shift of the SSP(0,1) resonance from its smooth film values is $\Delta\epsilon^{(\text{EM})} \approx -3.6$. Comparing $\Delta\epsilon^{(\text{EM})}$ to $\Delta\epsilon^{(\text{ES})}$, we conclude that only about one-half of the red-shift of the absorption peak from the position of the smooth film SSP(1, 0) resonance can be attributed to the radiative effect. The second half is a purely electrostatic effect that occurs due to hybridization of the electrostatic SSP resonances in the presence of a large hole.

No identification with one of the smooth film SSPs can be made for the LSP resonance at $\lambda = 10.5 \mu\text{m}$ shown in figure 1. In fact, this surface wave resonance, highly localized near the hole perimeter, can be thought of as an even-parity ‘defect state’ created by the presence of a single hole in a negative- ϵ film. Because the frequency range for which $-1 < \epsilon(\omega) < 0$ is a stop-band for even-parity propagating SPs, the even-parity LSP can exist in this frequency range alone. Because of the localized nature of the LSP, its frequency is insensitive to the proximity of other holes (i.e. to the period L) but is sensitive to the aspect ratio of the hole and even to the radius of curvature of hole edge. As may be seen in figure 1, frequencies of the three red resonances ($\lambda > 10.6 \mu\text{m}$) are located in the $\text{Re}[\epsilon_{\text{SiC}}] < -1$ band and are all dependent on L . In contrast, the blue resonance ($\lambda_{\text{loc}} \approx 10.5 \mu\text{m}$) belongs to the $-1 < \text{Re}[\epsilon_{\text{SiC}}] < 0$ range and is period independent. Another striking difference between the red and blue resonances is that the former are very delocalized, while the latter is strongly localized near the hole (see the two insets to figure 1).

To summarize, we have theoretically explained transmission and absorption anomalies of sub-wavelength hole arrays by introducing the effective permittivity of a perforated

membrane with a complex frequency dependence caused by resonant coupling to surface phonon polaritons. Two types of phonon polariton resonances are theoretically uncovered: (i) delocalized modes related to slow surface polaritons (SSPs) of a smooth film, and (ii) a localized surface polariton (LSP) of a single hole in the spectral range complementary to that of SSPs. We have also discussed the red-shift of the transmission/absorption maximum through a perforated film with large holes from the position corresponding to the frequency of a smooth film SSP. This diameter-dependent shift comes from the combination of two factors: (a) a purely electrostatic effect of the resonant frequency shift of a perforated film, and (b) a purely electromagnetic effect of radiation through a finite-diameter hole. The relative importance of the latter phenomenon increases with the hole diameter.

4. Spectroscopy of perforated SiC membranes: experimental procedures and results

In this section experimental measurements of the EOT and enhanced optical absorption (EOA) in a sub-wavelength array of holes drilled in air-bridged (suspended) SiC films is described. All experiments are done in the mid-infrared frequency range ($7\ \mu\text{m} < \lambda < 16\ \mu\text{m}$), which encompasses the *reststrahlen* band of SiC inside which $\epsilon < 0$. The FTIR micro-spectroscope used in this study collects all transmitted and reflected light, enabling us to separately compute scattered and absorbed fractions of the incident light in a manner similar to an earlier study [24] of a hole array in a metal screen. The high accuracy of our measurements and the utilization of an infrared polarizer enable us to separate the peaks of EOT and EOA for both s and p polarizations. Moreover, by rotating the stage on which the perforated film is positioned (see figure 9), the incidence plane of the beam with respect to the rows of the array could be changed for each polarization. This additional flexibility enables us, for the first time, to experimentally demonstrate a high (up to a factor of two) anisotropy with respect to different orientations of the incidence plane. Even for the appreciably sub- λ arrays ($L = 7\ \mu\text{m}$, $\lambda \approx 12\ \mu\text{m}$) used in this study, this high anisotropy is observed for fairly small ($\approx 20^\circ$) incidence angles. Depending on the incidence plane orientation, absorption spectra are shown to exhibit single- or double-peaked transmission spectra.

4.1. Fabrication of hole arrays in SiC membranes

Two-dimensional arrays of holes were fabricated in suspended SiC membranes. The starting material for the membrane is a 458 nm thick single-crystalline 3C-SiC film heteroepitaxially grown on a 0.5 mm thick Si(100) wafer. SiC epitaxy is performed in an RF induction-heated reactor using a two-step, carbonization-based atmospheric pressure chemical vapour deposition process detailed elsewhere [28]. Silane and propane are used as process gases and hydrogen is used as the carrier gas. Epitaxial growth is performed at a susceptor temperature of about 1330 °C. SiC films grown using this process have a uniform orientation (100) across each wafer, as indicated by x-ray diffraction. Transmission electron microscopy and selective area diffraction analysis indicates that the films are single crystalline.

The following steps were followed in the creation of SiC membranes. Layers of 5 μm SiO₂ were deposited on both sides of the Si wafer in a high-temperature furnace (600 °C). The surface opposite to SiC was coated with a 1 μm layer of photoresist (Clariant AZ5209), after which 1 mm \times 1 mm windows were exposed to UV by contact optical lithography (Karl Suss mask aligner). After resist exposure (60 s), development (45 s in Clariant AZ726 developer) and post-bake (20 min), the samples were placed in a BOE solution (2 h), completely removing SiO₂ from the SiC side of the wafer and forming 1 mm \times 1 mm openings in the SiO₂ mask on the opposite side. After removing photoresist in Piranha solution, we performed Si etching in a 35% KOH solution (at 80 °C for 10 h). The etch process of Si by KOH was anisotropic, forming an angle of 35.3° from normal. Upon etching through the Si wafer (0.5 mm), 0.35 mm \times 0.35 mm SiC membranes were exposed. High selectivity of the KOH Si etch with respect to SiC (260 000:1) ensured that SiC membranes were relatively unaffected by the etch process.

A dual-beam FIB/SEM system (FEI DB235) was used to create hole arrays in SiC membranes: FIB utilized Ga⁺ ions to mill through SiC while SEM was used to observe results and produce micrographs. Several types of hole arrays have been fabricated. Here we discuss the square array sample with a hole diameter of 2 μm and a lattice spacing of 7 μm . Using an ion current of 300 pA, it took nearly 4 h to fabricate a single 150 μm \times 150 μm hole array with the aforementioned parameters.

4.2. Apparatus and SiC film characterization

A Perkin Elmer spectrum GX AutoImage FTIR microscope at the University of Texas at Dallas was used to measure the transmission and reflection coefficients of samples in the 600–1500 cm⁻¹ spectral range. The schematic of the FTIR optics is shown in figure 8. Spectral resolution of the FTIR was set to 1 cm⁻¹, and the spatial range was a (100 μm)² region at the sample plane, described in detail below. The image of the sample was picked up by a video camera within the microscope and the sample position was monitored on a computer screen. Samples were moved in horizontal (x , y) and vertical (z) directions and rotated about the z -axis. To define the spatial orientation of the sample, a nine-hole cluster was fabricated above the sample, seen in figure 6. To calibrate reflection measurements, a high-quality aluminium mirror (CVI) was used. A wire-mesh polarizer (ISP Optics, 2400 grooves mm⁻¹) was used to analyse radiation in the FTIR.

The IR beam is directed by Cassegrain optics as schematically shown (reflection mode) in figure 8, solely comprised of reflective surfaces. To determine the actual geometrical characteristics of the probing IR beam, its cross-section was scanned by small apertures in two planes—the focal plane and 557 μm above the focus. Pinholes with diameters of 20 and 40 μm were used for focal plane and above focal plane scans, respectively. The beam distribution in the focal plane was nearly square with a 100 μm edge length. The beam characteristics are described by the two spherical coordinate angles θ and φ defined in figure 9. By analysing the IR beam intensity distribution for both planes, shown in figure 7, we have determined that the incidence angle range is

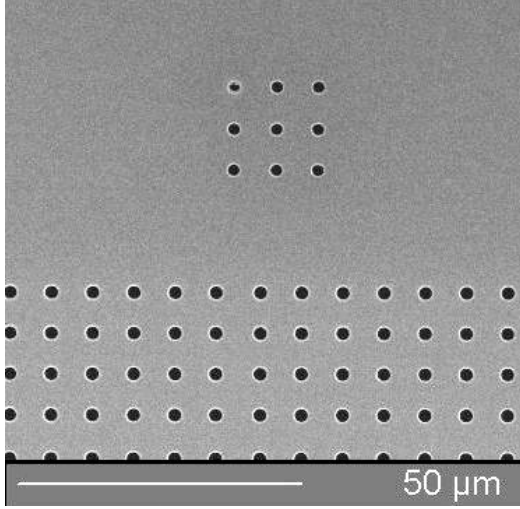


Figure 6. A nine-hole cluster was fabricated above the hole array to define the spatial orientation of the sample. This SEM micrograph serves to show the $7\ \mu\text{m}$ period array of $2\ \mu\text{m}$ diameter holes, with the reference cluster approximately $20\ \mu\text{m}$ from the array edge.

$\theta = 22^\circ \pm 4^\circ$. The azimuthal range of φ defining the orientation of the incidence planes with respect to rows of holes is equal to $\approx \pm 10^\circ$. Note that $\varphi = 0^\circ$ corresponds to the incidence plane parallel to the rows of holes.

Unusual spectra from edge effects have been observed [29] in experiments with finite-sized arrays, where larger-than-array beams probe additional areas of non-perforated materials. Our arrays can be considered ‘infinite’ because the probing radiation is contained in an area smaller than the array, ensuring that any result observed comes from the holes rather than from edge effects. The hole arrays in SiC cover an area of $(150\ \mu\text{m})^2$; when rotated 45° about the z -axis, a square sample space must be greater than $(\sqrt{2} \times 100\ \mu\text{m})^2$ or about $(142\ \mu\text{m})^2$ in size to remain within the original $(100\ \mu\text{m})^2$ window of study. Samples of area $(150\ \mu\text{m})^2$ can therefore undergo 360° rotation for complete illumination under any sample orientation, a condition necessary if studying angular anisotropy. In this work, the sample was studied under four orientations: $\varphi = 0^\circ, 45^\circ, 90^\circ, 135^\circ$.

Although optical constants of bulk SiC are well documented [30], those of a thin epitaxially grown film need to be determined experimentally. Discrepancy between thin film and bulk SiC occurs because of the high stress in the films grown at high temperature and poor control of the growth process. For example, there is a high probability of unintentional nitrogen doping during growth that results in a high carrier concentration. By examining transmission data, we have verified that the frequencies $\omega_{\text{LO}} = 972\ \text{cm}^{-1}$ ($\lambda_{\text{LO}} = 10.288\ \mu\text{m}$) and $\omega_{\text{TO}} = 796\ \text{cm}^{-1}$ ($\lambda_{\text{TO}} = 12.563\ \mu\text{m}$) reported for bulk SiC [30] are in excellent agreement with our data.

To account for the likely unintentional doping of SiC, we have added an extra conductivity term in equation (8). We then performed a three-parametric least-square fitting between our transmission spectra and transmittance given by equations (9) in order to determine the three unknown optical constants Γ , σ and ϵ_∞ . Transmittances of both s and p polarizations ($T_{s,p}$)

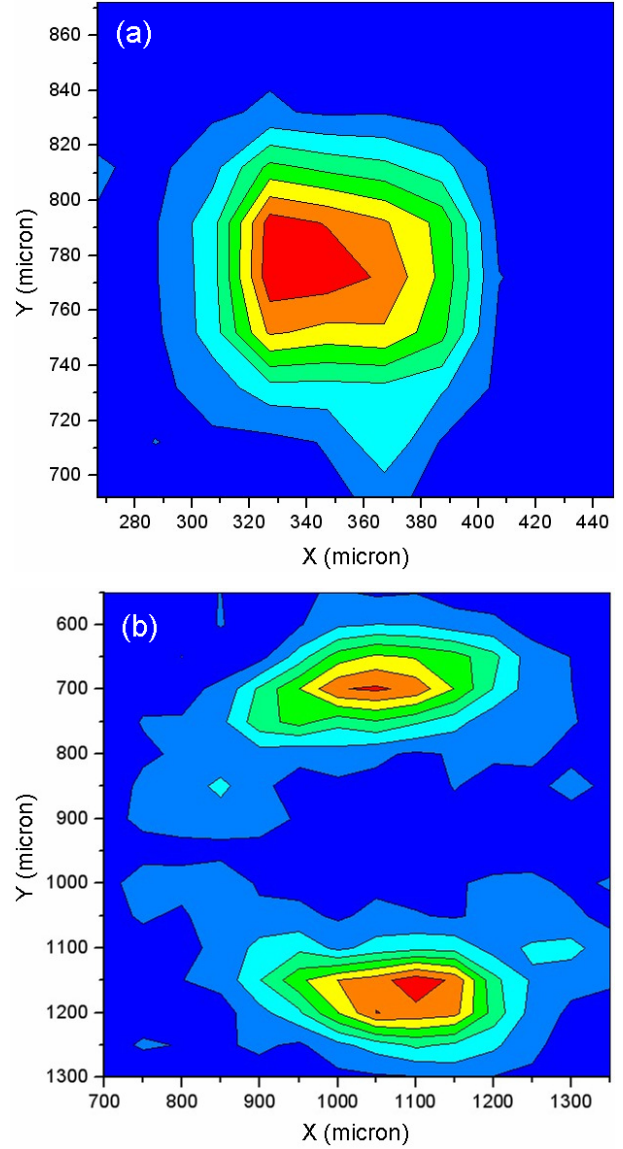


Figure 7. FTIR beam intensity profiles in the x - y plane. (a) Focal plane; (b) $557\ \mu\text{m}$ above the focal plane. The origin of x - y coordinates is arbitrary. In the focal plane, the beam is contained within a $(100\ \mu\text{m})^2$ region.

were included in the least-square minimization. The following constants gave the best fit: $\Gamma = 5.25\ \text{cm}^{-1}$, $\sigma = 346.2\ \text{cm}^{-1}$, $\epsilon_\infty = 4.71$. Theoretical fits (dashed lines) and experimental measurements (solid lines) for both polarizations plotted in figure 10 show good agreement.

4.3. Experimental results

Using the dielectric permittivity $\epsilon(\omega)$ of SiC given by equation (8) with experimentally determined optical constants, we compared theoretical (from the first-principles FEFD simulations) and measured reflection $R(\lambda)$, transmission $T(\lambda)$, and absorption $A(\lambda) = 1 - R - T$ coefficients. The results obtained for an s-polarized incident beam with the incidence plane corresponding to $\varphi = 0^\circ$ (parallel to rows of holes) are plotted in figure 11 for the $7\ \mu\text{m}$ period array of $2\ \mu\text{m}$ diameter

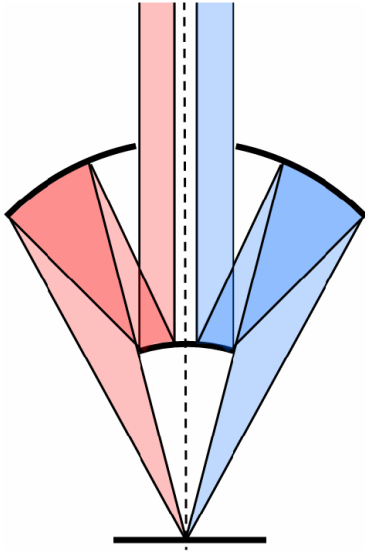


Figure 8. Utilizing reflective Cassegrain optics, the FTIR focuses radiation on the sample at non-zero incidence (not to scale). In reflection mode, incident radiation (red, left) reflects from the sample (blue, right) and is analysed by the detector. In transmission mode, two beams come from the bottom, pass through the sample and are collected above.

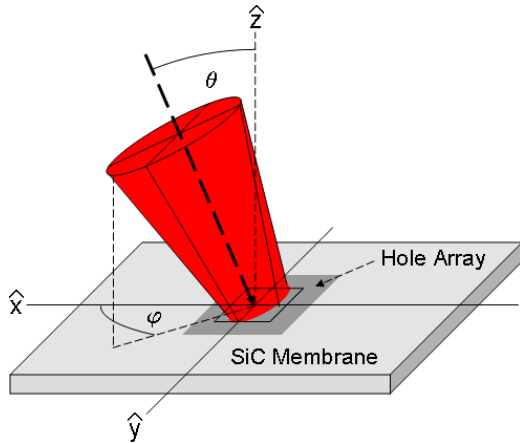


Figure 9. Schematic diagram of the FTIR beam incident upon the hole array (not to scale). The beam characteristics are described by spherical coordinates: θ denotes the polar angle from the z -axis (normal incidence) and φ denotes the azimuthal angle in the x - y plane (SiC surface) from the x -axis, which is attached to a row of holes. The value of φ shown on this plot visualizes the maximum azimuthal deviation of rays from the centre of the beam.

holes. Incidence angle $\theta = 22^\circ$ was assumed for numerical simulations. Given finite spread in θ and φ for realistic experimental conditions, the agreement between theory and experiment is good. Both $T(\lambda)$ and $R(\lambda)$ exhibit characteristic kinks at the frequencies corresponding to excitation of SPPs. The shapes of these kinks are reminiscent of Fano resonances. They represent interference between radiation transmitted through the film (continuum state) with the radiation re-emitted by SPPs through the holes (discrete state). In most experiments to date, identification of the continuous and discrete states was elusive [31], mostly because of the close proximity between

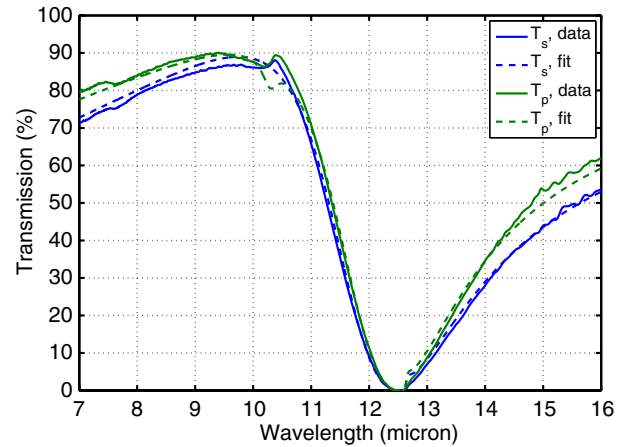


Figure 10. FTIR transmission spectra (in s- and p-polarized light) of a non-perforated 458 nm SiC film (solid lines) around the polaritonic resonance of $\approx 12.6 \mu\text{m}$, and the spectra corresponding to the best parametric fit obtained as described in the text (dashed lines).

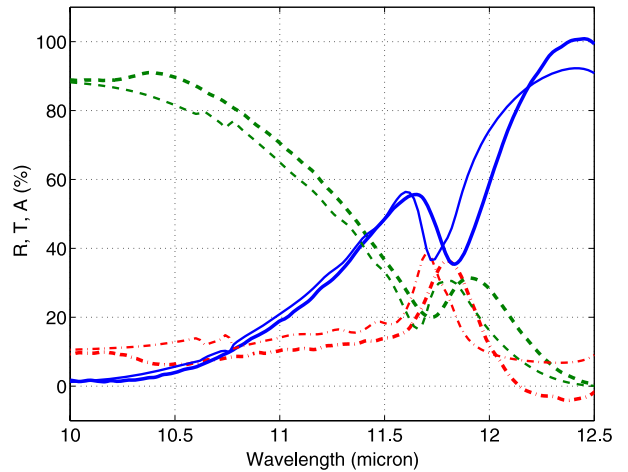


Figure 11. Spectra of the total reflection, transmission and absorption in solid, dashed, and dashed-dotted lines respectively, for the $7 \mu\text{m}$ period array of $2 \mu\text{m}$ diameter holes under s-polarized light and with $\varphi = 0$ sample orientation. The experimental FTIR results (thick lines) are in agreement with simulation results (thin lines) for angle of incidence $\theta = 20^\circ$.

Wood's anomalies and SPP resonances. In our experiment there is no ambiguity in identifying the dominant continuum state due to optical transparency of the film. Nor is the identification of slow surface polaritons as discrete states ambiguous because they are well separated from Wood's anomalies. In fact, our spectra are taken for the $10.5 \mu\text{m} < \lambda < 12.5 \mu\text{m}$ *reststrahlen* frequency band of SiC, inside which $\epsilon_{\text{SiC}} < 0$. Wood's anomalies corresponding to $\lambda \approx L = 7 \mu\text{m}$ are clearly outside the spectral range of our experiments.

Experimental results shown in figure 11 (thick lines) demonstrate that transmission peaks correlate with the absorption peaks (as has been previously noted [24]) because both are related to the excitation of SPPs. In full agreement with FEFD simulation results shown in figure 11 (thin lines) and theory presented in section 2, the transmission peak is red-shifted from the absorption peak. To our knowledge, this is the first experimental observation of this frequency shift.

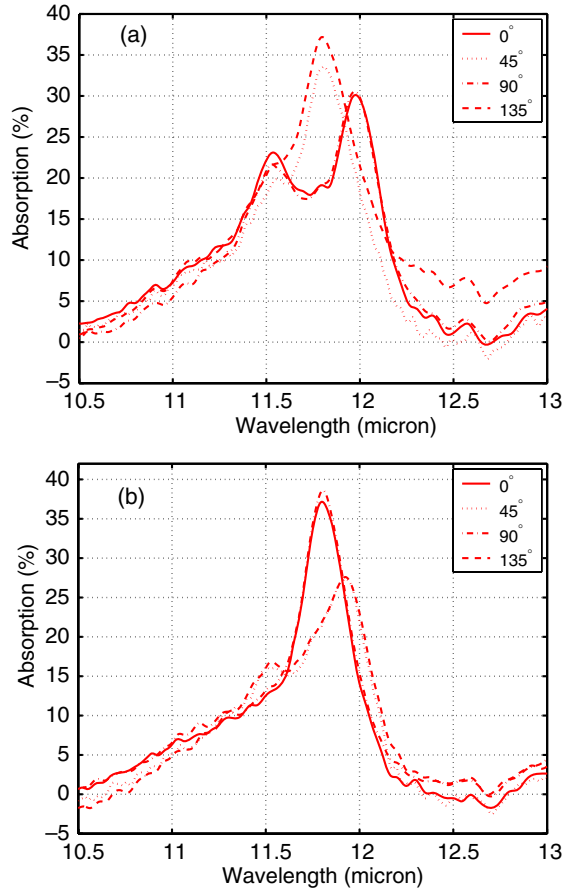


Figure 12. Absorption spectra for the $7\ \mu\text{m}$ period array of $2\ \mu\text{m}$ diameter holes under (a) p-polarized radiation and (b) s-polarized radiation with non-perforated film spectra subtracted. To study angular anisotropy, the sample was rotated in the x - y plane in increments of 45° from 0° to 135° .

While most hole array studies involve *optically thick* (several times thicker than the skin depth) films, our *optically thin* samples allow non-vanishing transmission without any perforations. Although it was generally believed that optical thinness allows for transmission significant enough to deem holes unnecessary [3], figure 11 demonstrated that holes modify transmission spectra to such an extent that optical thinness is not a detriment. This modification occurs in a specific spectral range where surface polaritons are excited. To quantify the role of the holes, spectra of smooth SiC membranes located next to the perforation windows were measured and subtracted from the corresponding hole array spectra.

Spectra were taken under various conditions: s- and p-polarized IR radiation was used, and the sample was rotated in the x - y plane in 45° increments from 0° to 135° . The results in figures 12 and 13 are displayed in a manner to show angular anisotropy at fixed polarizations. It is seen that spectra change considerably when the sample is rotated from a parallel to diagonal orientation. For the p-polarized radiation with the incidence plane parallel to rows or columns ($\phi = 0^\circ$ or $\phi = 90^\circ$) both absorption (figures 12 (a)) and transmission (figure 13 (a)) exhibit double-peaked spectra. Qualitatively, this is related to the fact that the radiation,

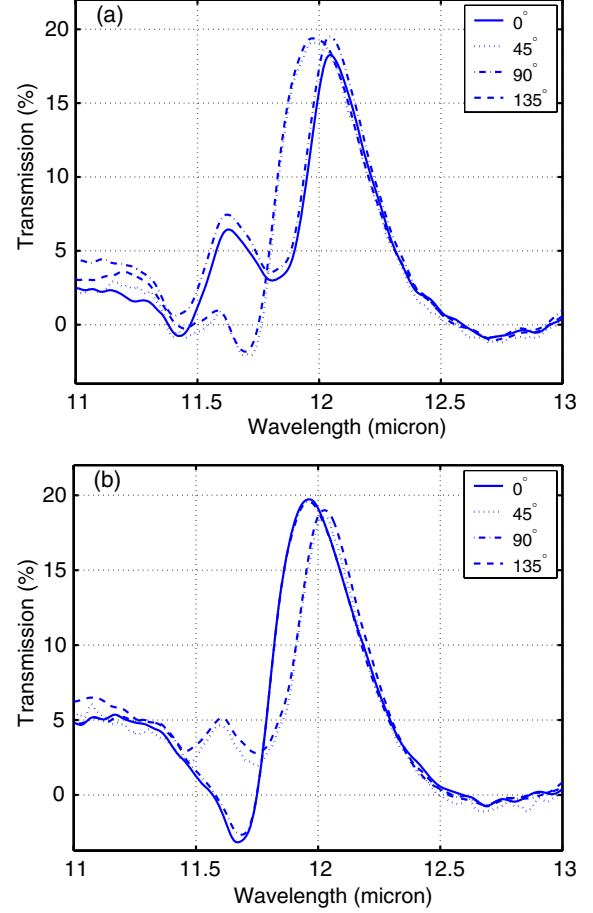


Figure 13. Transmission spectra for the $7\ \mu\text{m}$ period array of $2\ \mu\text{m}$ diameter holes under (a) p-polarized radiation and (b) s-polarized radiation with non-perforated film spectra subtracted. To study angular anisotropy, the sample was rotated in the x - y plane in increments of 45° from 0° to 135° .

incident at an angle θ , can strongly couple to two SSPs with $k_{\pm}^{\text{SSP}} = 2\pi/L \pm \sin\theta\omega/c$. When the sample is rotated by 45° , the two peaks are too close to each other to be clearly distinguished. An opposite trend is observed in s polarization, as shown in figures 12(b) and 13(b): for $\phi = 0^\circ, 90^\circ$ there is a single absorption/transmission peak which splits into two when the sample is rotated by 45° . As expected, the $A(\lambda)$ and $T(\lambda)$ spectra are invariant with respect to a 90° rotation as confirmed by all plots within figures 12 and 13—a reassuring sign that the array holes were precisely placed to form a symmetric, evenly spaced lattice. Through the aforementioned 90° sample symmetry, an absorption or transmission spectrum will alternate between one and two peaks with rotation; this effect could be used in spectral filtering applications and for the identification and alignment of sample orientation.

Another interesting and potentially useful property of perforated hole arrays is their extraordinary birefringence with respect to light polarization. For a given sample orientation ($\phi = 0^\circ$ in figure 14 and $\phi = 45^\circ$ in figure 15) transmission and absorption spectra are plotted for s and p polarizations and compared with the corresponding numerical simulations. For both sample orientations, we find that a very significant birefringence in transmission of order $|T_s - T_p| \approx 20\%$ can

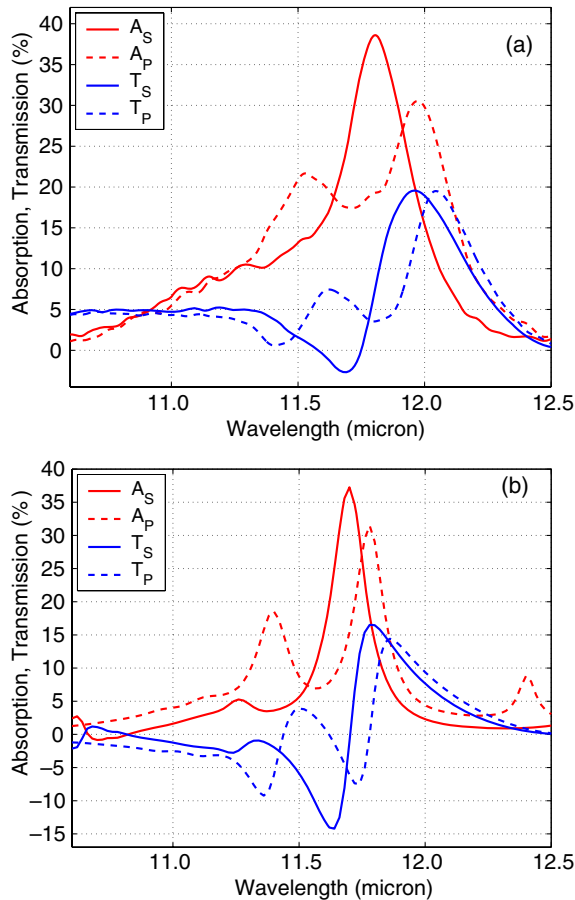


Figure 14. Absorption and transmission spectra from (a) experiments and (b) simulations for s and p polarization at 0° sample orientation with non-perforated film spectra subtracted. Absorption peak splitting, observed when changing from s to p polarization, is clearly seen in (a) and (b) with similar split peak-to-peak magnitude and frequency differences. Transmission spectra for both s and p polarization follow nearly identical paths in (a) and (b).

be obtained for the two polarizations. This is significantly higher than the birefringence from the unperforated film (about 5%) as shown from figure 10. Enhanced s/p-polarization birefringence can be explained using the qualitative band diagram of SPPs [24]. Such enhanced birefringence will manifest itself in polarization conversion (e.g. from linear to elliptical) if the incident polarization is a superposition of s and p polarizations. Experimental indications of polarization rotation have already been found in earlier experiments [4, 25], although the connection to s/p-polarization birefringence has not been made.

Experimental results shown in figures 14(a) and 15(a) show a very good qualitative agreement when compared to their simulation counterparts shown in figures 14(b) and 15(b). For the $\varphi = 0^\circ$ sample orientation, s-polarized light results in a strong single absorption/transmission peak, splitting to twin peaks with p-polarized light, seen in figure 14. The peak splitting in figure 14 (a) found experimentally is verified by simulations and shown in figure 14 (b) with similar split peak-to-peak magnitude and frequency differences. Peak splitting in p polarization and the lack thereof in s polarization has been noted earlier [24] for thick metallic films.

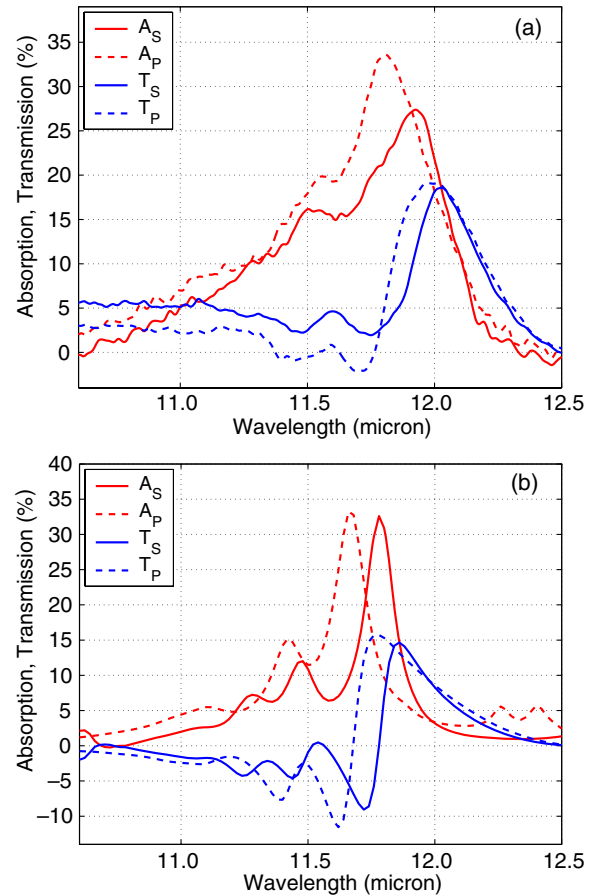


Figure 15. Absorption and transmission spectra from (a) experiments and (b) simulations for s and p polarization at 45° sample orientation with non-perforated film spectra subtracted. While the main s and p polarization absorption peak magnitudes differ in (a) but not (b), both sets display a similar frequency shift and maintain similar relative shapes. Transmission spectra also follow nearly identical paths in (a) and (b) for corresponding s and p polarizations.

We also find a significant s/p-polarization birefringence for the $\varphi = 45^\circ$ sample orientation. Although the quantitative agreement between the experimental and theoretical results for the sample orientation of $\varphi = 45^\circ$ shown in figures 15(a) and (b), respectively, is less impressive than that for the $\varphi = 0^\circ$ sample orientation, figures 14(a) and (b), the qualitative agreement is quite good. Both the primary and much smaller secondary absorption/transmission peaks in both polarizations are seen in experiments and simulations. The primary peaks in A_P and T_P are shifted to frequencies higher than those of A_S and T_S , an experimental result (figure 15 (a)) reproduced through simulation (figure 15 (b)). While the peak magnitude difference between A_P and A_S in figure 15 (a) is not seen in figure 15 (b), the frequency shift of $0.12 \mu\text{m}$ occurs in both experiments and simulations. The numerical difference between electromagnetic simulations and experimental results can be caused by several factors: uncertainty in the dielectric function of perforated SiC (see figure 10), significant spread in the angles of incidence at the sample, and insufficiently precise decomposition of optical spectra into s and p polarization caused by uncertainties of the beam propagation inside the FTIR device. Future experiments with infrared laser sources

will allow us to better control angles of incidence and polarization and improve quantitative agreement with the theory.

5. Conclusions

In conclusion, we have theoretically and experimentally investigated the phenomenon of enhanced optical transmission (EOT) in the mid-infrared through a square array of sub-wavelength round holes milled in an optically thin polaritonic (SiC) membrane. We have theoretically demonstrated and experimentally verified that EOT is accompanied by a slightly blue-shifted absorption peak corresponding to enhanced optical absorption (EOA). Both EOT and EOA were shown to be caused by the excitation of quasi-electrostatic resonances of the film that can be traced to even-parity surface phonon polaritons of the smooth film. Enhanced absorption and transmission as high as nearly 40% each have been shown for the arrays in which holes occupied only 6% of the total area. Such high absorbance indicates that perforated SiC films can be used as highly efficient tunable thermal radiation sources.

The major differences of our experiments from the earlier EOT experiments are as follows: (a) optically thin *phonon-polaritonic* films (SiC) are used; (b) SiC films are suspended (air-bridged, i.e., there is no underlying substrate) and (c) the hole array is essentially sub-wavelength (the ratios of the period L and diameter D to wavelength λ are $L/\lambda \approx 0.6$ and $D/\lambda \approx 0.2$). This choice of the experimental parameters enabled us, for the first time, to definitively eliminate diffraction and interference effects (Wood's anomalies, 'spoof polaritons', waveguide resonances, and quasi-bound modes) as being responsible for EOT/EOA, and to demonstrate that both phenomena are caused by the excitation of surface phonon polaritons. Because of the sub-wavelength nature of the perforated hole array, we have been able to model it as a metamaterial described by the effective (quasi-static) dielectric permittivity obtained using electrostatic simulations. For the first time, we have investigated the dependence of EOT and EOA on both incident wave polarization (s and p) and incidence plane orientation with respect to the rows of the holes. The high degree of anisotropy with respect to the incidence plane orientation has been demonstrated and theoretically explained. Strong polarization dependence can be utilized in polarization converters while strong anisotropy can be used as a diagnostic of the film orientation in sensing applications.

Acknowledgments

This work is supported by the ARO MURI W911NF-04-01-0203, AFOSR MURI FA9550-06-01-0279, and DARPA contract HR0011-05-C-0068. We gratefully acknowledge Drs

A Aliev and A A Zakhidov for their assistance with FTIR micro-spectroscopy.

References

- [1] Bethe H A 1944 *Phys. Rev.* **66** 163
- [2] Ebbesen T W, Lezec H J, Ghaemi H F, Thio T and Wolff P A 1998 *Nature* **391** 667
- [3] Genet C and Ebbesen T W 2007 *Nature* **445** 39
- [4] Tetz K A, Pang L and Fainman Y 2006 *Opt. Lett.* **31** 1528
- [5] Coe J V, Williams S M, Rodriguez K R, Teeters-Kennedy S, Sudnitsyn A and Hrovat F 2006 *Anal. Chem.* **78** (5) 1385–90
- [6] Stewart M E, Mack N H, Malyarchuk V, Soares J A N T, Lee T-W, Gray S K, Nuzzo R G and Rogers J A 2006 *Proc. Natl Acad. Sci.* **103** 17143
- [7] Cao Q and Lalanne P 2002 *Phys. Rev. Lett.* **88** 057403
- [8] Lezec H and Thio T 2004 *Opt. Express* **12** 3629
- [9] Martin-Moreno L, Garcia-Vidal F J, Lezec H, Pellerin K M, Thio T, Pendry J B and Ebbesen T W 2001 *Phys. Rev. Lett.* **86** 1114
- [10] García de Abajo F J, Gómez-Medina R and Sáenz J J 2005 *Phys. Rev. E* **72** 016608
- [11] Gomez Rivas J, Schotsch C, Haring Bolivar P and Kurtz H 2003 *Phys. Rev. B* **68** 201306(R)
- [12] Lockyear M J, Hibbins A P and Sambles J R 2004 *Appl. Phys. Lett.* **84** 2040
- [13] Pendry J B, Martin-Moreno L and Garcia-Vidal F J 2004 *Science* **305** 847
- [14] Genet C, van Exter M P and Woerdman J P 2003 *Opt. Commun.* **225** 331
- [15] Sarrazin M, Vigneron J P and Vigoureux J-M 2003 *Phys. Rev. B* **67** 085415
- [16] Bergman D and Stroud D 1992 *Solid State Phys.* **46** 147
- [17] Stockman M I, Faleev S V and Bergman D J 2001 *Phys. Rev. Lett.* **87** 167401
- [18] Shvets G and Urzhumov Y 2004 *Phys. Rev. Lett.* **93** 243902
- [19] Zhikov V V 1994 *Homogenization of Differential Operators and Integral Functionals* (New York: Springer)
- [20] Milton G W 2002 *The Theory of Composites* (Cambridge: Cambridge University Press)
- [21] Bergman D and Dunn K-J 1992 *Phys. Rev. B* **45** 13262
- [22] Stroud D 1979 *Phys. Rev. B* **19** 1783
- [23] Mayergoyz I D, Fredkin D R and Zhang Z 2005 *Phys. Rev. B* **72** 155412
- [24] Barnes W L, Murray W A, Dintiger J, Devaux E and Ebbesen T W 2004 *Phys. Rev. Lett.* **92** 107401
- [25] Altewischer E, van Exter M P and Woerdman J P 2003 *J. Opt. Soc. Am. B* **20** 1927–31
- [26] Ghaemi H F, Thio T, Grupp D E, Ebbesen T W and Lezec H J 1998 *Phys. Rev. B* **58** 6779
- [27] Salomon L, Grillot F, Zayats A V and de Fornel F 2001 *Phys. Rev. Lett.* **86** 1110
- [28] Zorman C A, Fleischman A J, Dewa A S, Mehregany M, Jacob C and Pirouz P 1995 *J. Appl. Phys.* **78** 5136
- [29] Degiron A, Lezec H J, Barnes W L and Ebbesen T W 2002 *Appl. Phys. Lett.* **81** 4327
- [30] Olego D and Cardona M 1982 *Phys. Rev. B* **25** 3889
- [31] Chang S-H, Gray S K and Schatz G C 2005 *Opt. Express* **13** 3150